

# Mesoscopic simulation of non-ideal fluids with self-tuning of the equation of state

Carlos E. Colosqui\*    Giacomo Falcucci<sup>†</sup>    Stefano Ubertini<sup>‡</sup>

Sauro Succi<sup>§</sup>

December 23, 2011

December 23, 2011

## Abstract

A dynamic optimization strategy is presented to generate customized equations of state (EOS) for the numerical simulation of non-ideal fluids at high density ratio. While stable branches of the analytical EOS are preserved, the spinodal region is self-tuned during the simulation, in order to compensate for numerical errors caused by discretization in phase space.

---

\*Dept. of Chemical Engineering, Princeton University, Princeton, NJ 08544, USA;  
E-mail: colosqui@princeton.edu;

<sup>†</sup>Department of Technologies, University of Naples Parthenope, Naples, Italy;  
E-mail: giacomo.falcucci@uniparthenope.it;

<sup>‡</sup>Department of Technologies, University of Naples Parthenope, Naples, Italy;  
E-mail: stefano.ubertini@uniparthenope.it;

<sup>§</sup>Istituto per le Applicazioni del Calcolo, IAC-CNR, Rome, Italy;  
E-mail: succi@iac.cnr.it; corresponding author.

The employed EOS permits to readily set the sound speeds for the gas and liquid phases, thus allowing stable simulation with high density (1:10 to 1:1000) and compressibility ratios (250:1–25000:1). The present technique is demonstrated for lattice Boltzmann simulation of (free-space) multiphase systems with flat and circular interfaces.

## 1 Introduction

Mesoscopic approaches, such as the lattice-Boltzmann (LB) method, allow physical modelling at an intermediate level between atomic/molecular interactions and a continuum representation (<sup>1</sup>). Hence, mesoscopic models are suitable for describing complex fluid systems, where the microscopic (atomistic) dynamics plays a non-trivial role in determining macroscopic (observable) quantities. Given the practical importance of such multiscale fluid systems (e.g. multiphase flows, microflows, nanofluids, soft matter systems) in science and engineering, LB continues to cross scientific research boundaries into novel applications across disciplines (<sup>2</sup>).

As the number of technical applications for LB rapidly grows, it is essential to elucidate actual capability and limitations of the methods employed. Another point of interest, is determining the compatibility between relatively new LB models and long-established continuum theories. A successful LB technique for multiphase, due to Shan and Chen (SC), is to model atomistic interactions via pseudo-internal forces, which are defined as a function of pseudo-potentials

(<sup>3</sup>). Pseudo-potentials, commonly determined by local macroscopic variables like mass density, represent coarse-grained approximations of the actual microscopic interactions.

**The pseudo-potential approach does not attempt to model microscopic correlations or details of the dynamics at molecular time/length scale. These microscopic phenomena determine the complex dependence of transport coefficients on thermodynamic variables or observables such as temperature, pressure, concentration, etc. The employed mesoscopic approach is intended to produce hydrodynamic equations with the correct functional form. Mapping these equations to real systems must be accomplished by very carefully tuning the relevant dimensionless groups (e.g. Capillary number, Ohnesorge number, etc. ) for the particular problem of interest.**

At continuum level, the functional form of the pseudo-potential employed can be a priori designed to produce a desired macroscopic behaviour. For the multiphase fluid systems of interest in this work, pseudo-potentials are defined in order to produce a desired equation of state (EOS) and a finite surface tension at the vapour-liquid interface. However, several limitations have been pointed out for the numerical implementation of the SC approach, most notably the fact that stable phase-separation is hard to achieve for density ratios above 30 – 50. In addition, the SC EOS, at least in its original formulation, leads to a smaller sound speed in the liquid than in the vapour phase; this is clearly non-physical and likely a cause of numerical instability as well (<sup>4</sup>).

In LB simulation, the employed EOS determines the pseudo-internal fluid

forces resulting from density difference between neighbouring nodes. Under appropriate conditions, a finite-size (or diffuse) interface arises, due to the interplay between modelled pseudo-internal forces and diffusion processes. The coexistence properties (e.g. bulk density and pressure) numerically obtained, as well as the density profile and thickness of the simulated interface, are not only determined by the functional form of the EOS, but also by the properties of the lattice employed (e.g. thermal speed) and diverse discretization effects. Whenever discretization effects remain negligible, the LB simulation agrees closely with (continuum) thermodynamic predictions for the mechanical and chemical equilibrium conditions determined by the EOS (<sup>1,5</sup>). This is commonly the case when the ratio of the bulk densities of the fluid phases is relatively modest, i.e around 10 – 30. However, several fluids of practical interest (e.g. water-air mixtures) exhibit density contrasts that span over several orders of magnitude. Furthermore, meso/macroscopic structures (e.g. liquid drop or colloid radius) have characteristic length-scales that are usually many orders of magnitude larger than the interface thickness. Hence, it is a common necessity to deal with large density jumps across extremely thin interfaces; e.g. for air-water systems at standard pressure-temperature conditions, the interface thickness is in the nanometer scale, while the density ratio is 1:1000. In these challenging situations for diffuse-interface methods, the numerical interface is usually heavily under-resolved, for the sake of computational tractability. When the interface is under-resolved, discretization errors (in both configuration and phase space) necessarily cause deviations from the coexistence properties, as computed via continuum thermodynamics (<sup>4,5</sup>). In

this work we propose and demonstrate LB procedures for the robust simulation of multiphase flows at high-density ratios. The key proposed concept is to adjust the numerical EOS in the unstable branch, i.e. within the spinodal region. This technique allows to compensate for numerical errors originated at the discretized interface, without affecting bulk properties.

The LB model in this work employs projection in Hermite space of the non-equilibrium distribution (<sup>6-8</sup>); this additional feature becomes crucial when large spatial gradients are present. This simple procedure removes errors due to numerical integration, thus leading to numerical solutions that are independent of the lattice-flow alignment (<sup>9</sup>). The vast majority of LB models are in essence diffuse-interface methods. Although this work focuses on LB models using pseudo-potential approaches, the methodology proposed in this paper can be applied to most other models, e.g free-energy based LB methods (<sup>10</sup>), which exhibit the same issues in dealing with high density ratios.

The present paper is organized as follows. First, we review the basic elements of the Hermite-compliant formulation of the continuum and lattice Boltzmann-BGK equations. Subsequently, we illustrate the procedure for the customization of mechanically and thermodynamically consistent EOS, achieving large density ratios, with higher sound speed in the liquid than in the vapour phase. The procedure is then numerically demonstrated for the case of two-dimensional flat interfaces and circular droplets, both at rest and in motion. Finally, a brief summary of the results concludes the paper.

## 2 Boltzmann BGK model

We begin by considering the Boltzmann–BGK (Bhatnagar-Gross-Krook) equation for a single component fluid:

$$\frac{\partial f}{\partial t} + \mathbf{v} \cdot \nabla f = -\frac{f - f^{eq}}{\tau} + \frac{\delta f}{\delta t}. \quad (1)$$

Here, we have defined  $\theta = k_B T / m = c_s^2$ , adopting a unit molecular mass  $m = 1$ . The relation  $\theta = c_s^2$ , i.e. thermal speed equal to the sound speed, only holds for an ideal gas, and shall be generalized to the case of a non-ideal fluid in the sequel. The left hand side represents molecular free-streaming, while the right hand side collects the effect of hard-core collisions, relaxing the system towards the local equilibrium  $f^{eq}$ , and mean-field, soft-core interactions, denoted by  $\delta f / \delta t$ , which are responsible for non-ideal fluid-behaviour. The equilibrium distribution is given by a local Maxwellian:

$$f^{eq}(\mathbf{x}, \mathbf{v}, t) = \frac{\rho}{(2\pi\theta)^{\frac{D}{2}}} \exp\left[-\frac{(\mathbf{v} - \mathbf{u})^2}{2\theta}\right] \quad (2)$$

with  $D$  being the velocity space dimension ( $\mathbf{v} = v_k \mathbf{e}_k$ ;  $k = 1, \dots, D$ ). The term  $\delta f / \delta t = -\mathbf{g} \cdot \nabla_{\mathbf{v}} f$  ( $\mathbf{g}$  represents the sum of external and internal forces per unit mass), and accounts for the effect of external force fields and internal soft-core interactions. We shall focus on isothermal flow regimes, for which  $\theta \simeq \text{const}$ . Hence, the basic variables employed for the hydrodynamic description are mass density  $\rho$  and fluid velocity  $\mathbf{u}$ , which are obtained as moments of the distribution

function  $f$ :

$$\int f(\mathbf{x}, \mathbf{v}, t) d\mathbf{v} = \rho(\mathbf{x}, t) \quad (3)$$

$$\int f(\mathbf{x}, \mathbf{v}, t) \mathbf{v} d\mathbf{v} = \rho \mathbf{u}(\mathbf{x}, t) \quad (4)$$

In addition, the inclusion of convective and dissipative effects, also requires consideration of the kinetic momentum-flux tensor:

$$\int f(\mathbf{x}, \mathbf{v}, t) \mathbf{v} \mathbf{v} d\mathbf{v} = \rho [\mathbf{u}(\mathbf{x}, t) \mathbf{u}(\mathbf{x}, t) + \theta \mathbf{I}] + \mathbf{P}_{\text{neq}}. \quad (5)$$

The subscript *neq* indicates the non-equilibrium component which is responsible for momentum diffusivity and dissipative effects in the fluid. For the case of non-ideal fluids, the potential-energy component of the momentum flux tensor also needs to be considered, as it will be detailed shortly.

## 2.1 Hydrodynamic Approximation in $\mathbb{H}^2$

From a mathematical standpoint, the lattice Boltzmann (LB) method is basically a finite-difference scheme. However, it has been recently shown that it can also be given a more rigorous formulation as Galerkin method<sup>(11)</sup> for approximate solution of the continuum Boltzmann-BGK. A so-called  $N$ -order LB model seeks for solution in a functional space  $\mathbb{H}^N$  spanned by the leading Hermite polynomials of order  $\leq N$  (i.e.  $f \in \mathbb{H}^N$ ). Conventional LB algorithms are not consistent with standard Galerkin procedures. In such procedures the actual Galerkin coefficients, determined by kinetic moments of the distribution function, must be

“evolved” in time in such a way as to keep the approximate solution within a desired function space all along the time evolution. It is to be noted that, starting from a distribution  $f \equiv f(\mathbf{x}, \mathbf{v}, t)$  belonging to  $\mathbb{H}^N$ , the post-advection distribution  $\hat{f}(\mathbf{x}, \mathbf{v}, t) \equiv f(\mathbf{x} - \mathbf{v}\Delta t, \mathbf{v}, t)$ , lies generally outside  $\mathbb{H}^N$ . A Taylor expansion in powers of the differential  $\Delta \mathbf{x} = \mathbf{v}\Delta t$  readily shows that  $\hat{f} \in \mathbb{H}^{N+k}$  ( $k \geq 1$ ) for non-vanishing spatial derivatives (i.e. in non-equilibrium conditions). Significant errors can be introduced when computing the moments of the distribution function if the polynomial degree of  $\hat{f}$  is larger than the algebraic degree of precision of the quadrature rule employed <sup>(6,7)</sup>. Therefore, projection of the post-advection distribution is critical for consistency with Galerkin procedures for which a rigorous convergence theory exists.

Since isothermal hydrodynamics is described by the first two kinetic moments, mass and momentum density, in this work we will employ the popular approximation in  $\mathbb{H}^2$ , given by the following (second-order) Hermite series:

$$f(\mathbf{x}, \mathbf{v}, t) = f^M(\mathbf{v}) \left[ M^{(0)} + \frac{1}{\theta} \mathbf{M}^{(1)} : \mathbf{v} + \frac{1}{2\theta^2} (\mathbf{M}^{(2)} - M^{(0)} \theta \mathbf{I}) : (\mathbf{v}\mathbf{v} - \theta \mathbf{I}) \right], \quad (6)$$

$$f^{eq}(\mathbf{x}, \mathbf{v}, t) = f^M(\mathbf{v}) \left[ M_{eq}^{(0)} + \frac{1}{\theta} \mathbf{M}_{eq}^{(1)} : \mathbf{v} + \frac{1}{2\theta^2} (\mathbf{M}_{eq}^{(2)} - M_{eq}^{(0)} \theta \mathbf{I}) : (\mathbf{v}\mathbf{v} - \theta \mathbf{I}) \right], \quad (7)$$

$$\frac{\delta f(\mathbf{x}, \mathbf{v}, t)}{\delta t} = f^M(\mathbf{v}) \left[ M_{\delta}^{(0)} + \frac{1}{\theta} \mathbf{M}_{\delta}^{(1)} : \mathbf{v} + \frac{1}{2\theta^2} (\mathbf{M}_{\delta}^{(2)} - M_{\delta}^{(0)} \theta \mathbf{I}) : (\mathbf{v}\mathbf{v} - \theta \mathbf{I}) \right]. \quad (8)$$

For compact notation we employ  $f^M = \exp(-\mathbf{v}^2/2\theta)/(2\pi\theta)^{3/2}$  and  $I_{\alpha\beta} = \delta_{\alpha\beta}$ . The relations above involve the  $n$ -order velocity moments

$$\mathbf{M}^{(n)}(\mathbf{x}, t) = \int f(\mathbf{x}, \mathbf{v}, t) \mathbf{v}^n d\mathbf{v} \quad (9)$$

and their equilibrium counterparts  $\mathbf{M}_{eq}^{(n)} = \int f^{eq} \mathbf{v}^n d\mathbf{v}$ ,  $\mathbf{M}_{\delta}^{(n)} = \int (\delta f / \delta t) \mathbf{v}^n d\mathbf{v}$ . Note that the symbol  $\mathbf{v}^n$  denotes a  $n$ -th order tensor; in component notation  $v_{\alpha_1} v_{\alpha_2} \dots v_{\alpha_n}$ .

For convenience, we rearrange Eq. (1) as follows:

$$\left( 1 + \tau \frac{\partial}{\partial t} \right) f + \tau \mathbf{v} \cdot \nabla f = f^{eq} + \tau \frac{\delta f}{\delta t}, \quad (10)$$

and then evaluate the zero- and first-order moment equations (i.e. mass and momentum equations):

$$\left( 1 + \tau \frac{\partial}{\partial t} \right) \mathbf{M}^{(0)} + \tau \nabla \cdot \mathbf{M}^{(1)} = \mathbf{M}_{eq}^{(0)} + \tau \mathbf{M}_{\delta}^{(0)}, \quad (11)$$

$$\left( 1 + \tau \frac{\partial}{\partial t} \right) \partial_t \mathbf{M}^{(1)} + \tau \nabla \cdot \mathbf{M}^{(2)} = \mathbf{M}_{eq}^{(1)} + \tau \mathbf{M}_{\delta}^{(1)}. \quad (12)$$

In order to obtain a closed system of governing equations, we must express the second-order moment  $\mathbf{M}^{(2)}$  in terms of lower-order moments or basic variables

(3–4). The moment equation for the second-order moment reads as follows:

$$\left(1 + \tau \frac{\partial}{\partial t}\right) \mathbf{M}^{(2)} = \mathbf{M}_{eq}^{(2)} + \tau \mathbf{M}_{\delta}^{(2)} - \tau \nabla \cdot \mathbf{M}^{(3)} \quad (13)$$

Clearly, this is not closed, due to the presence of the third-order moment  $\mathbf{M}^{(3)}$ . However, using Eq.(6) for  $f \in \mathbb{H}^2$ , we can readily compute the third-order moment in terms of the first-order one as follows:

$$M_{\alpha\beta\gamma}^{(3)}(\mathbf{x}, t) = \theta \left( M_{\alpha}^{(1)} \delta_{\beta\gamma} + M_{\beta}^{(1)} \delta_{\alpha\gamma} + M_{\gamma}^{(1)} \delta_{\alpha\beta} \right). \quad (14)$$

To arrive at this result, we have made use of the definition of the Hermite polynomials  $H_i^{(1)} = \xi_i$ ,  $H_{ijk}^{(3)} = [\xi_i \xi_j \xi_k - (\xi_i \delta_{jk} + \xi_j \delta_{ik} + \xi_k \delta_{ij})]$  ( $\xi = \mathbf{v}/c_s$ ), as well as of the orthogonality of the Hermite basis.

We then multiply Eq. (12) by  $(1 + \tau \partial_t)$  and use Eq. (14), to obtain the following closed equation for the first-order moment dynamics:

$$\begin{aligned} \left(1 + \tau \frac{\partial}{\partial t}\right)^2 \mathbf{M}^{(1)} &= \tau^2 \theta \nabla \cdot \mathbf{D}^{(1)} + \left(1 + \tau \frac{\partial}{\partial t}\right) \left( \mathbf{M}_{eq}^{(1)} + \tau \mathbf{M}_{\delta}^{(1)} \right) \\ &\quad - \tau \nabla \cdot \mathbf{M}_{eq}^{(2)} - \tau^2 \nabla \cdot \mathbf{M}_{\delta}^{(2)} \end{aligned} \quad (15)$$

where:

$$\mathbf{D}^{(1)} = \left[ \nabla \mathbf{M}^{(1)} + [\nabla \mathbf{M}^{(1)}]^T + \nabla \cdot \mathbf{M}^{(1)} \mathbf{I} \right] \quad (16)$$

is the deformation tensor associated with the current  $\mathbf{M}^{(1)} = \rho \mathbf{u}$  (see below). The

closed description given by Eqs. (11) and (15) provides an exact (within the second order Hermite representation) analytical description, to be matched by numerical solutions of the LB methods.

A few comments are in order. First, we note that the presence of the time-delay derivative  $(1 + \tau\partial_t)$ , makes this system second-order not only in space, but also in time, thereby preserving the hyperbolic nature of the original kinetic equation, a property clearly *not* shared by standard Navier-Stokes (NS) equations. In fact, the present formulation bears many similarities to the so-called telegraphers's equations (<sup>12,13</sup>), and has the capability of taking account of fast-dynamics phenomena which escape a purely Navier-Stokes description. Second, we note that, although no formal expansions about equilibrium state have been performed so far, the closure  $f \in \mathbb{H}^2$ , is de-facto equivalent to replacing the moment  $\mathbf{M}^{(3)}$  with its equilibrium expression. This approximation is necessary to retrieve hydrodynamics from kinetic theory, and it is commonly adopted in the derivation of the Navier-Stokes equations from LBE. However, the Hermite projection provides a sound mathematical basis for this approximation, which is why the algorithmic implementation must explicitly account for such a projection.

In the following section, we shall briefly revisit under which conditions, the Navier-Stokes equation for both ideal and non-ideal fluids, are attained from the present set of moment equations.

## 2.2 Continuum limit for an ideal fluid case

We now recast Eq. (15) in the more recognizable form in terms of (generalized) continuity and momentum equations. In particular, we shall discuss under which conditions the above equation leads to the *NS* equation. Evaluating the equilibrium moments given by Eq. (7) one obtains:

$$\mathbf{M}_{eq}^{(0)} = \mathbf{M}^{(0)} = \rho, \quad (17)$$

$$\mathbf{M}_{eq}^{(1)} = \mathbf{M}^{(1)} = \rho \mathbf{u}, \quad (18)$$

$$\mathbf{M}_{eq}^{(2)} = \rho \mathbf{u} \mathbf{u} + \rho \theta \mathbf{I} \neq \mathbf{M}^{(2)}. \quad (19)$$

The low-order moment dynamics given by Eqs. (11) and (15), delivers the following continuity and momentum equations:

$$\frac{\partial}{\partial t} \rho + \nabla \cdot (\rho \mathbf{u}) = \mathbf{M}_{\delta}^{(0)}, \quad (20)$$

$$\begin{aligned} \left(1 + \tau \frac{\partial}{\partial t}\right) \frac{\partial}{\partial t} \rho \mathbf{u} + \nabla \cdot (\rho \mathbf{u} \mathbf{u}) = & - \nabla \rho \theta + \left(1 + \tau \frac{\partial}{\partial t}\right) \mathbf{M}_{\delta}^{(1)} - \tau \nabla \cdot \mathbf{M}_{\delta}^{(2)} \\ & + \tau \theta \nabla \cdot \mathbf{D}^{(1)}. \end{aligned} \quad (21)$$

The first equation is easily recognized as the continuity equation, with a mass source term. Note that no adiabatic assumption  $\tau \partial_t \ll 1$  is required at the level of the continuity equation, because  $M^{(0)} = M_{eq}^{(0)}$ . The same is true for the momentum equation, since momentum is also conserved. Such adiabatic assumption is

usually invoked at the level of the second moment, which is not conserved. Here, however, since the full time-delay operator is retained, the only closure is to keep  $f$  within  $\mathbb{H}^2$ , with no adiabatic requirement,  $\tau|\partial_t M^{(2)}| \ll |M^{(2)} - M_{eq}^{(2)}|$ .

To forestall any confusion, by “adiabatic”, we imply here that “fast” modes are enslaved to the “slow” ones, with no specific reference to heat transport phenomena. In fact, since the equilibrium distribution is truncated to second order Hermite polynomials, our treatment does not include any heat transport effect, which is sometimes referred to as to “athermal” regime.

The first line in the r.h.s. of Eq. (21) includes the moments of the forcing term  $\delta f/\delta t$  that produce an effective pressure tensor  $\mathbf{P}$  in such way that

$$\nabla \cdot \mathbf{P} = \nabla \cdot \left[ \rho \theta \mathbf{I} + \tau \mathbf{M}_\delta^{(2)} \right] - \left( 1 + \tau \frac{\partial}{\partial t} \right) \mathbf{M}_\delta^{(1)}. \quad (22)$$

can accommodate a non-ideal equation of state. The second line in Eq. (21), where the closure takes place, requires a few additional comments. The deformation tensor  $\mathbf{D}^{(1)}$  reduces to the Galilean-invariant expression of the dissipative Navier-Stokes tensor of a compressible flow,

$$D_{NS} = \rho \left[ \frac{\nabla \mathbf{u} + [\nabla \mathbf{u}]^T}{2} - \frac{1}{3} (\nabla \cdot \mathbf{u}) \mathbf{I} \right], \quad (23)$$

only the limit where density gradients remain negligible as compared to the velocity gradients, that is,  $|\nabla \rho/\rho| \ll |\nabla \mathbf{u}|/|\mathbf{u}|$  (this condition is trivially satisfied under no-flow conditions). Since Galilean-invariance is manifestly built-in the BGK equation, through the dependence of the local equilibrium on the relative molec-

ular velocity  $\mathbf{v} - \mathbf{u}$ , lack of Galilean invariance is a consequence of the closure  $M^{(3)} \sim c_s^2 M^{(1)}$ . Indeed, since the local equilibrium entails an infinite expansion in the Mach number, the  $n$ -th coefficient of such an expansion being the  $n$ -th order (tensor) Hermite polynomials, it is clear that no finite-order projection in Hermite space can recover Galilean invariance in full, i.e. at all orders in the Mach number. This is a general problem of continuum kinetic theory, which is inherited by the LB formulation. Indeed, in order to retain Galilean invariance up to  $n$ -th order, isotropy of the corresponding  $n$ -th order lattice tensors is required, thus setting a high demand on the lattice symmetry and number of discrete speeds, which becomes rapidly incompatible with computational efficiency. The practical outcome is that, near steep interfaces, where  $w|\nabla\rho/\rho| \gg 1$ ,  $w$  being the interface width, many sources of inaccuracy inevitably arise. Given that these inaccuracies are virtually irreducible, the most effective strategy is to try not to eliminate them, but rather to keep them *confined* within the interface, i.e. prevent them not only from compromising numerical stability, but also from affecting the bulk properties of the fluid away from the interface. This is precisely the type of strategy presented in this work. To demonstrate that Navier-Stokes equations are approximated for near equilibrium conditions, we set  $\mathbf{M}_\delta^{(n)} = 0$  and employ the approximation that density gradients scale as  $\mathcal{O}(Ma^2)$ , (<sup>14</sup>). Provided such approximation holds, Eq. (21)

then becomes

$$\begin{aligned} \left(1 + \tau \frac{\partial}{\partial t}\right) \left[ \frac{\partial}{\partial t} \rho \mathbf{u} + \nabla \cdot (\rho \mathbf{u} \mathbf{u}) \right] = & - \left(1 + \tau \frac{\partial}{\partial t}\right) \nabla p \\ & + \nabla \cdot \mu \left[ \frac{\nabla \mathbf{u} + \nabla^T \mathbf{u}}{2} - \frac{1}{3} (\nabla \cdot \mathbf{u}) \mathbf{I} \right] + \mathcal{O}(u^3) \end{aligned} \quad (24)$$

where  $p = \theta \rho$  is the ideal EOS and  $\mu = \tau \theta \rho$  is the dynamic viscosity of the fluid. The equation above approaches the Navier-Stokes equation for momentum conservation only in the adiabatic limit  $|\tau \partial_t M^{(2)}| \ll |M^{(2)} - M_{eq}^{(2)}|$  and low Mach-number,  $Ma = u/\sqrt{\theta} \ll 1$ .

## 2.3 Force term implementations

The forcing term in the kinetic equation  $\delta f/\delta t$  can be implemented via different approximations (<sup>15-22</sup>) all equally conforming to low-order approximations of the momentum equation. Such different approximations, however, introduce different error terms in the higher-order moments  $\mathbf{M}_\delta^{(n)}$ , that have significant effects on the numerical stability of the LB algorithm. Below we briefly describe and compare two schemes that have been commonly employed.

### 2.3.1 Scheme I: Shifted equilibrium

In this scheme, the idea is that the force  $\mathbf{g}$  produces a momentum shift  $\tau \rho \mathbf{g}$  in the local equilibrium distribution (<sup>15,16</sup>), which is then centred upon the new shifted velocity  $\mathbf{u}^* = \mathbf{u} + \tau \mathbf{g}$  in Eq. (2). Hence, the approximation to the forcing term

becomes

$$\frac{\delta f}{\delta t} = \frac{1}{\tau} [f^{eq}(\rho, \mathbf{u} + \tau \mathbf{g}) - f^{eq}(\rho, \mathbf{u})] = f^M(\mathbf{v}) \left[ \frac{1}{\theta} \rho \mathbf{g} : \mathbf{v} + \frac{1}{2\theta^2} \rho (2\mathbf{u}\mathbf{g} + \tau \mathbf{g}\mathbf{g}) : (\mathbf{v}\mathbf{v} - \theta \mathbf{I}) \right]. \quad (25)$$

Up to second order in the Froude number,  $Fr = \tau |\mathbf{g}| / \sqrt{\theta}$ , the shifted equilibria correspond to introducing a supplementary diffusion term in velocity space, of the form  $\frac{\tau}{2} \mathbf{g}\mathbf{g} : \nabla_v \nabla_v$ , which improves numerical stability. However, at higher orders, lack of sufficient lattice isotropy implies the emergence of Galilean-invariance violating terms, which compromise the accuracy and, at sufficiently high Froude numbers, even the stability of the method.

### 2.3.2 Scheme II: Method of exact differences

A scheme which allows larger Froude numbers (<sup>4</sup>), reads as follows:

$$\frac{\delta f}{\delta t} = \frac{1}{\Delta t} [f^{eq}(\rho, \mathbf{u} + \Delta t \mathbf{g}) - f^{eq}(\rho, \mathbf{u})] = f^M(\mathbf{v}) \left[ \frac{1}{\theta} \rho \mathbf{g} : \mathbf{v} + \frac{1}{2\theta^2} \rho (2\mathbf{u}\mathbf{g} + \Delta t \mathbf{g}\mathbf{g}) : (\mathbf{v}\mathbf{v} - \theta \mathbf{I}) \right]. \quad (26)$$

This corresponds to the exact difference that takes the equilibrium distribution  $f^{eq}(\rho, \mathbf{u})$  to a new equilibrium state where the local momentum is  $\rho \mathbf{u} + \mathbf{g} \Delta t$  in a time step  $\Delta t$ . Recalling Eq. (8), it is readily seen that the scheme gives  $\mathbf{M}_\delta^{(1)} = \rho \mathbf{g}$  and  $\mathbf{M}_\delta^{(2)} = \rho (2\mathbf{u}\mathbf{g} + \Delta t \mathbf{g}\mathbf{g})$ . **This implementation, which becomes exact in equilibrium conditions ( $f = f^{eq}$ ), removes the dependence of the non-Galilean terms on the relaxation time  $\tau$ . This is found to increase the numerical stability of the scheme, thereby permitting to reach higher Froude numbers.**

**Although we adopt the method of exact differences, the proposed self-tuning of the equation of state can in principle improve the accuracy of numerical simulations using alternative approximations for the force term. By accuracy, we refer here to close agreement between numerical results and continuum thermodynamics calculations for phase equilibrium. The method of exact differences was favoured as it allows to employ a wider range of relaxation times and, thus, fluid viscosities.**

## 2.4 Non-ideal fluid behaviour

The hydrodynamic description rendered by LB is given by the moment equations (20)–(21), which contain a (non-isotropic) pressure tensor  $P$  defined in Eq. (22). A possible path to model multiphase flow is to approximate an available macroscopic description by directly defining the velocity moments  $\mathbf{M}_{eq}^{(n)}$  and  $\mathbf{M}_{\delta}^{(n)}$  ( $n = 0, 1, 2$ ) that determine the equilibrium distribution (7) and forcing term (8). This is precisely the approach adopted by so-called free energy methods (23). In this work, we follow the Shan-Chen formulation where microscopic interactions forces  $\mathbf{g}$  are modelled in order to produce non-ideal fluid behaviour.

It is physically insightful to recast the net internal force  $\mathbf{g}$  as a spatial convolution over a suitable pseudo-potential  $\psi(\mathbf{x}, t) = \psi(\rho(\mathbf{x}, t))$  so that

$$\rho \mathbf{g}(\mathbf{x}, t) = -\psi(\mathbf{x}, t) \int \frac{d}{d\mathbf{r}} w(|\mathbf{r}|) \psi(\mathbf{x} + \mathbf{r}, t) d\mathbf{r}. \quad (27)$$

The Gaussian convolution kernel  $w(|\mathbf{r}|) = \exp(-|\mathbf{r}|^2/2\kappa\theta)/(2\pi\kappa\theta)^{2/3}$ , a heuris-

tic replacement for the two-body radial correlation function, satisfies the following normalizations,  $\int w(|\mathbf{r}|) d\mathbf{r} = 1$  and  $\int w(|\mathbf{r}|)\mathbf{r}\mathbf{r} d\mathbf{r} = \kappa\theta\mathbf{I}$ . It is worth noticing that  $\sqrt{\kappa\theta}$ , where  $\theta = k_B T/m$  is the thermal energy (per unit mass) and  $\sqrt{\kappa}$  has units of time, determines the (mesoscopic) length scale  $\kappa\theta$  for the decay of the pair correlation.

By Taylor-expanding the r.h.s of Eq. (27), we obtain:

$$\rho\mathbf{g}(\mathbf{x},t) = \nabla \cdot \left[ \left( \frac{\psi^2}{2} + \frac{\kappa\theta}{2}\psi\nabla^2\psi + \frac{\kappa\theta}{4}|\nabla\psi|^2 \right) \mathbf{I} - \frac{\kappa\theta}{2}\nabla\psi\nabla\psi \right] + \mathcal{O}(|\nabla^4|) \quad (28)$$

When implementing the exact-difference scheme described in Sec. 2.3, the divergence of the pressure tensor (22) becomes

$$\nabla \cdot \mathbf{P} = \nabla\rho\theta - \left( 1 + \tau\frac{\partial}{\partial t} \right) \rho\mathbf{g} + \tau\nabla \cdot [\rho(2\mathbf{u}\mathbf{g} + \Delta t\mathbf{g}\mathbf{g})]. \quad (29)$$

The equation above for the pressure tensor makes clear that the modelled microscopic interactions produce the following: (i) non-ideal fluid behaviour; given by an excess pressure  $p^*(\rho) = -\frac{\psi^2(\rho)}{2}$  in the isotropic component of  $\mathbf{P}$  and non-local terms that can be associated to a free-energy excess; and (ii) error terms which are the result of the (second-order) approximation employed for the forcing  $\delta f/\delta t$ . Note that the isotropic component of  $\tau\Delta t\mathbf{g}\mathbf{g}$  increases mechanical stability ( $\partial p/\partial\rho > 0$ ) and thus improves the numerical stability. The force implementation also produces an incorrect shift in temperature  $\theta$  and the ensuing violation of kinetic energy conservation<sup>(24)</sup>; this is precisely one of the deficiencies that we sought to rectify by adjusting the EOS in the unstable branch where

the force magnitude  $|\mathbf{g}|$  is large. Note that the result in Eq. (29) is quite general for LB models; e.g. the pressure tensor for the shifted-equilibrium scheme is readily recovered replacing  $\Delta t$  by  $\tau$ .

#### 2.4.1 Pseudo-potential and equation of state

In the limit of small Froude numbers  $Fr = \tau|\mathbf{g}|/\sqrt{\theta} \ll 1$ , the functional form of the pseudo-potential  $\psi(\rho)$  determines the equilibrium static pressure the phase bulk

$$p_{EOS}(\rho, \theta) = \rho\theta + p^*(\rho) = \rho\theta - \frac{\psi^2(\rho)}{2}. \quad (30)$$

The sign convention employed in this derivation makes straightforward the physical interpretation of the fact that thermal diffusion is opposed by the action of (attractive) long-range forces. It also becomes clearer that, without accounting explicitly for repulsive (short-range) interactions, a dominant thermal diffusion is critical for mechanical stability.

By properly choosing the functional form of the pseudo-potential  $\psi(\rho)$ , non-trivial equations of state supporting phase transitions are generated. Following the present derivation, one recovers the original Shan-Chen EOS by adopting  $\psi(\rho) = i\sqrt{G\theta}(1 - e^{-\rho})$  (where  $i = \sqrt{-1}$ ) and  $G$  the coupling strength of the Shan-Chen pseudo-potential.

The resulting EOS would yield a phase transition at the critical density  $\rho_c = \log 2$  for  $|G| > G_c = 4$ . The Shan-Chen pseudo-potential has many virtues and some pitfalls too. Among others, it can be readily checked that the sound speed,  $c_s^2 = \partial p / \partial \rho$ ,

is higher in the vapour than in the liquid phase. Although harmless for many applications, such feature is clearly non-physical and can lead to numerical instability.

In this work we take the approach upside down, i.e. we first choose the form of the non-ideal EOS  $p = p(\rho)$ , and then define the pseudo-potential according to:

$$\psi(\mathbf{x}, t) = \sqrt{2[\rho\theta - p_{EOS}(\rho, \theta)]} \quad (31)$$

consistently with the definition of  $-\psi^2$  as the excess pressure due to non-ideal interactions. In order to ensure numerical stability the magnitude of the speed of sound (in both stable and unstable phases) must be such that  $c_s^2 \leq \theta$ ; this condition also ensures a positive value of the term inside the square root in Eq. (30).

Before quitting this section, it is worth mentioning that other lattice-based methods for complex fluid have been recently developed <sup>(25)</sup>, based on the microscopic description of the interacting system of underlying molecules <sup>(26,27)</sup>.

### 3 Hermite-projected lattice Boltzmann method

Conventional LB methods resort to discretization in velocity space and operator splitting techniques. Hence, the conventional LB algorithm evolves a discrete set of lattice distributions  $\{f_i; i = 1, Q\}$  in two steps: advection  $\hat{f}_i(\mathbf{x} + \mathbf{v}_i\Delta t, t) = f_i(\mathbf{x}, t)$  and collision  $f_i(\mathbf{x}, t + \Delta t) = \hat{f}_i(\mathbf{x}, t) - [\hat{f}_i(\mathbf{x}, t) - f_i^{eq}] \Delta t / \tau$ . As usual,  $\mathbf{v}_i$  denotes the set of discrete velocities associated with the given lattice formulation. An appealing feature of the employed (second-order) Hermite-projected model is that the algorithm proceeds along the same lines as the conventional scheme, with an

additional projection step after the advection step (6,7):

$$f_{P_i}^{ne} = f^M(\mathbf{v}_i) \frac{1}{2\theta^2} \mathbf{P}_{neq} : (\mathbf{v}_i \mathbf{v}_i - \theta \mathbf{I}). \quad (32)$$

The (non-equilibrium) second-order moment  $\mathbf{P}_{neq}$  defined in Eq. (5) is computed using the post-advection distributions  $\mathbf{P}_{neq} = \sum w_i (\hat{f}_i - f^{eq}) \mathbf{v}_i \mathbf{v}_i$  ( $i = 1, Q$ ); note that owing to orthogonality of the Hermite basis the numerical integration will be exact provided that the algebraic degree of precision of the quadrature rule is  $\geq 4$ . The projected  $f_{P_i}^{ne}$  distribution is then employed to compute the collision step

$$f_i(\mathbf{x} + \mathbf{v}_i, t + \Delta t) = f_i^{eq}(\rho, \mathbf{u} + \mathbf{g}\Delta t) + \left(1 - \frac{\Delta t}{\tau}\right) f_{P_i}^{ne} \quad (33)$$

where non-ideal interactions are introduced by means of the exact-differences scheme in Eq. (26). The expression for the local force is

$$\rho \mathbf{g}(\mathbf{x}, t) = \psi(\mathbf{x}, t) \sum_{i=1}^Q w_i \mathbf{r}_i \psi(\mathbf{x} + \mathbf{r}_i, t). \quad (34)$$

given by the discrete form of Eq. (27) for the lattice and Gauss-Hermite (G-H) quadrature employed. For this work, we adopted  $\Delta t = \kappa = 1$ , while  $\mathbf{r}_i = \mathbf{v}_i \Delta t$  and  $w_i$  are given in Tables 1–2.

Projecting the post-advection distribution back onto the  $\mathbb{H}^2$  space, we reconstruct a *new* non-equilibrium distribution in Eq. (33) that lies entirely within  $\mathbb{H}^{(2)}$ . This practice is equivalent to “dealiasing” or filtering away the so-called *ghost* modes (8,16) that are inherent to the LB representation for matters of symmetry.

$\mathbf{c}_i/\sqrt{\theta}^a$	states	$w_i$
$(\pm 1, 0), (0, \pm 1)$	1–4	1/12
$(\pm 1, \pm 1)$	5–8	2/27
$(\pm 2, 0), (\pm 2, 0)$	9–12	7/360
$(\pm 2, \pm 2)$	13–16	1/432
$(\pm 3, 0), (0, \pm 3)$	17–20	1/1620
$(0, 0)$	21	91/324

<sup>a</sup>Lattice constant:  $\theta = k_B T / m = 2/3$

Table 1: Model Parameters D2Q21

### 3.1 High-order lattices

A so-called high-order lattice improves the discretization in velocity space by enlarging the number  $Q$  of discrete velocities  $\{\mathbf{v}_i; i = 1, Q\}$ . As a consequence, the maximum algebraic degree of precision of the associated Gauss-Hermite quadrature rule increases while higher-order moment isotropy and rotational symmetry are satisfied. The model used in this study employs a lattice consisting of 39 discrete speeds in three-dimensions (D3Q39). When the third dimension is quenched to just two periodic planes, the effective two-dimensional simulation takes place on the 21 discrete velocity lattice (D2Q21) shown in Figure 1. The abscissae and corresponding weights for the D3Q39 and D2Q21 are given in Tables 1–2. These lattices give a seventh-order algebraic precision ( $d = 7$ ) and satisfy moment isotropy up to the sixth-order (<sup>28</sup>). We chose higher-order lattices (D3Q39, D2Q21) over low-order versions (e.g D2Q9, D3Q27) due to their comparatively better performance in reducing spurious currents and other numerical artefacts at

$\mathbf{v}_i/\sqrt{\theta}^a$	states	$w_i$
$(\pm 1, 0, 0), (0, \pm 1, 0), (0, 0, \pm 1)$	1–6	1/12
$(\pm 1, \pm 1, \pm 1)$	7–14	1/12
$(\pm 2, 0, 0), (0, \pm 2, 0), (0, 0, \pm 2)$	15–20	1/27
$(\pm 2, \pm 2, \pm 2)$	21–32	2/135
$(\pm 3, 0, 0), (0, \pm 3, 0), (0, 0, \pm 3)$	33–38	1/432
$(0, 0, 0)$	39	1/1620

<sup>a</sup>Lattice constant:  $\theta = k_B T/m = 2/3$ ,  $c_s = \sqrt{2/3}$

Table 2: Model Parameters D3Q39

the vapour-liquid interface. Among other reasons, this favourable behaviour is attributed to a sixth-order moment isotropy supported by the enlarged set of lattice links [see Figure 1]. This feature allows to retain isotropy of fifth-order spatial derivatives in the discrete gradient operator (34) employed for the approximation of the internal forces (<sup>11</sup>).

## 4 Customizing the optimal EOS

In the previous sections we have outlined the basic technical aspects of the Hermite-compliant LB scheme used in this work. Next, we discuss a lattice-independent strategy to improve compliance with thermo-mechanical consistency requirements.

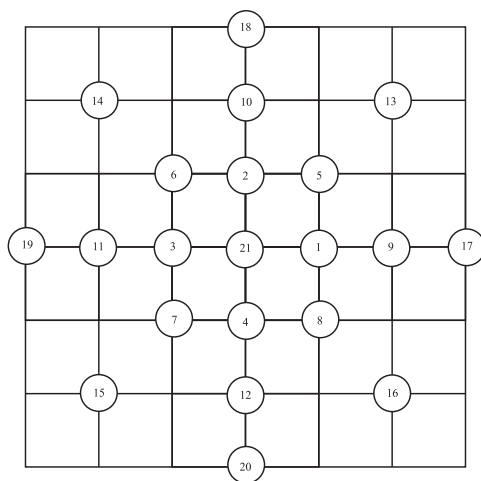


Figure 1: The D2Q21 lattice (a 2D projection of D3Q39). This lattice family satisfies moment isotropy up to the sixth-order. The discrete gradient operator implemented on these lattices retains isotropy up to the fifth-order spatial derivatives.

We begin by proposing a simple piecewise linear EOS

$$p(\rho) = \begin{cases} \rho \theta_V & \text{if } \rho \leq \rho_1 \\ \rho_1 \theta_V + (\rho - \rho_1) \theta_M & \text{if } \rho_1 < \rho \leq \rho_2 \\ \rho_1 \theta_V + (\rho_2 - \rho_1) \theta_M + (\rho - \rho_2) \theta_L & \text{if } \rho > \rho_2 \end{cases} \quad (35)$$

This EOS is uniquely defined by a set of five free parameters: (i) the coexistence vapour density  $\rho_V$ , (ii) the density ratio  $R = \rho_L/\rho_V$ , (iii) the (vapour-phase) speed-of-sound  $\sqrt{\theta_V} = \sqrt{(dp/d\rho)_V}$ , (iv) the (liquid-phase) speed-of-sound  $\sqrt{\theta_L} = \sqrt{(\partial p/\partial \rho)_L}$ , and (v) the slope  $\theta_S = (\partial p/\partial \rho)_S$  in the unstable branch (i.e. within the spinodal region). The unknown variables  $\rho_1$  and  $\rho_2$ , defining the the spinodal points, are readily obtained by solving the set of the two equations; one for determining me-

$R=\rho_L/\rho_V$	$\rho_V$	$\rho_1$	$\rho_2$	$\alpha_1$	$\alpha_2$
10	1	5.32	8.88	3.0	1.6–1.97
100	1	34.29	83.59	3.0	0.65–.88
1000	1	240.82	806.09	3.0	0.362–0.467

Table 3: EOS and perturbation parameters employed in our simulations. Different quasi-Newton methods tested in this work converged to the reported range of values of  $\alpha_2$  when varying the relaxation time  $\tau=1.0$ – $2.0$ .

chanical equilibrium

$$\int_{\rho_V}^{\rho_L} dp = (\rho_1 - \rho_V)\theta_V + (\rho_2 - \rho_1)\theta_S + (\rho_L - \rho_2)\theta_L = 0, \quad (36)$$

and other for chemical equilibrium

$$\int_{\rho_V}^{\rho_L} \frac{1}{\rho} dp = \log(\rho_1/\rho_V)\theta_V + \log(\rho_2/\rho_1)\theta_S + \log(\rho_L/\rho_2)\theta_L = 0. \quad (37)$$

#### 4.1 Discretization effects and perturbations in the unstable branch

As described in previous sections, numerical inaccuracies and truncation errors become significant for the large Froude numbers that are required in practice for simulation of large density ratios. The most immediate consequence is that the vapour and liquid densities numerically obtained for phase equilibrium can significantly differ from their continuum counterparts given by solution of Eqs. (36)-(37).

Compliance with continuum thermodynamics at high density ratios, may require impractical grid resolutions and/or come at the expense of the simplicity of the algorithm; e.g. adaptive meshes, interface tracking, and implicit schemes may be required. On a positive side, the largest numerical errors are majorly produced within the steepest regions of the interface where the pressure-density curve falls within the unstable branch ( $\rho_1 \leq \rho \leq \rho_2$ ) of the EOS where  $(\partial p / \partial \rho)_T < 0$ . Given that the unstable branch is experimentally inaccessible, one is naturally led to consider modifications of this branch aimed at minimizing the numerical errors. To implement this concept, we employ a modified EOS  $p(\rho)_{LB} = p(\rho) + \delta p$  where an analytical perturbation  $\delta p$  takes again the form of a piecewise-linear function:

$$\delta p(\rho, \alpha_1, \alpha_2) = \begin{cases} 0 & \text{if } \rho \leq \rho_1 \\ p_M \times \frac{\rho - \rho_1}{\rho_M - \rho_1} & \text{if } \rho_1 < \rho \leq \rho_M \\ p_M \times \frac{\rho - \rho_2}{\rho_M - \rho_2} & \text{if } \rho_M < \rho \leq \rho_2 \\ 0 & \text{if } \rho > \rho_2 \end{cases} \quad (38)$$

with  $p_M = \alpha_1(\rho_1 - \rho_2)\theta_S$  and  $\rho_M = \rho_1 + \alpha_2(\rho_2 - \rho_1)$ . The perturbation is uniquely determined by the parameters  $(\alpha_1, \alpha_2)$  that define the position  $\rho_M$  and magnitude of the maximum perturbation pressure  $p_M$  [see Figure 2]. The rationale for perturbing the unstable branch is that, for a given density profile  $\rho(\mathbf{x})$ , the slope of the EOS determines the magnitude of the internal forces  $\rho \mathbf{g}(\mathbf{x}) \sim -(\partial p / \partial \rho) \nabla \rho$  and thus the work done at crossing the interface. It is easily seen that positive values of the perturbation  $p_M$  produce a reduction of the internal force magnitude

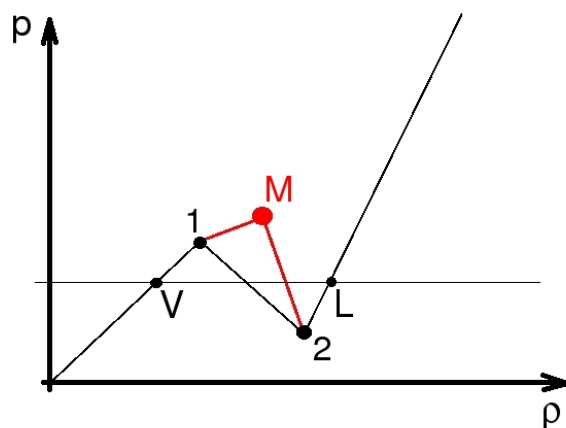


Figure 2: Piecewise EOS. Solid line (black):  $p(\rho)$  targeted EOS for continuum limit. Top-hat line (Red):  $p(\rho)_{LB} = p(\rho) + \delta p$  modified EOS for LB simulation.

toward the vapour side of the spinodal, and an increase toward the liquid side.

To illustrate the effects of the proposed perturbation on the unstable branch, we present in Figure 3 simulation results for a flat interface using the equation of state in Table 3 for  $\rho_L=100$  and  $\rho_V=1$ . It is worth to notice that the employed EOS, with a discontinuity in its first derivative, is extremely adverse for numerical discretization. As a consequence, employing the EOS without the proposed perturbation leads to vapour phase density  $\rho_V^{LB} < 1.0$  significantly smaller than expected; this occurs while the expected liquid phase density  $\rho_L^{LB} \simeq 100$  is recovered. As reported in previous works<sup>(4,5)</sup>, the coexistence value in the vapour phase is the quantity most sensitive to numerical inaccuracies.

As shown in Figures 3a–b, different combinations of perturbation parameters  $(\alpha_1, \alpha_2)$  can effectively compensate for numerical inaccuracies so that  $\rho_V^{LB} = 1$  (while  $\rho_L^{LB} = 100$ ). Varying  $\rho_M(\alpha_2)$  redistributes the work done by internal forces,

i.e. free energy excess in the inter-phase region, allowing to adjust equilibrium density on the vapour phase as reported in Figure 3c.

## 4.2 Self-tuning and discrete phase equilibrium

At the level of the lattice dynamics there are two simple processes; “thermal” diffusion  $\theta \nabla \rho(\mathbf{x})$ , modelled by advection-collision in the lattice, and a local momentum change driven by a force field  $\mathbf{g}\{\rho(\mathbf{x})\}$  that emulates long-range interactions. The interplay of these two modelled processes determine the actual coexistence densities  $\rho_L^{LB}$  and  $\rho_V^{LB}$  at which phase equilibrium is established in simulation; in general  $\rho_L^{LB} \neq \rho_L$  and  $\rho_V^{LB} \neq \rho_V$  due to diverse discretization errors in the pressure tensor (29). As demonstrated above, different corrections to the EOS in the unstable branch can optimize the agreement of numerical results with continuum thermodynamics. In what follows we describe one of many possible strategies to compute “*on the fly*” the optimal perturbation parameters. A typical manifold of optimal parameters is shown in Figure 3a, for a fixed value of  $\alpha_1$  (i.e. amplitude  $p_M$  of the perturbation) within the proper range there will be one value of  $\alpha_2$  that produces the expected coexistence densities. More general, multi-parametric optimization, schemes could also be conceived. For the sake of simplicity, in this work we shall confine our attention to the minimal two-parameter family of piecewise linear perturbations.

Based on the considerations above we attempt to find the parameter  $\alpha_2$ , given

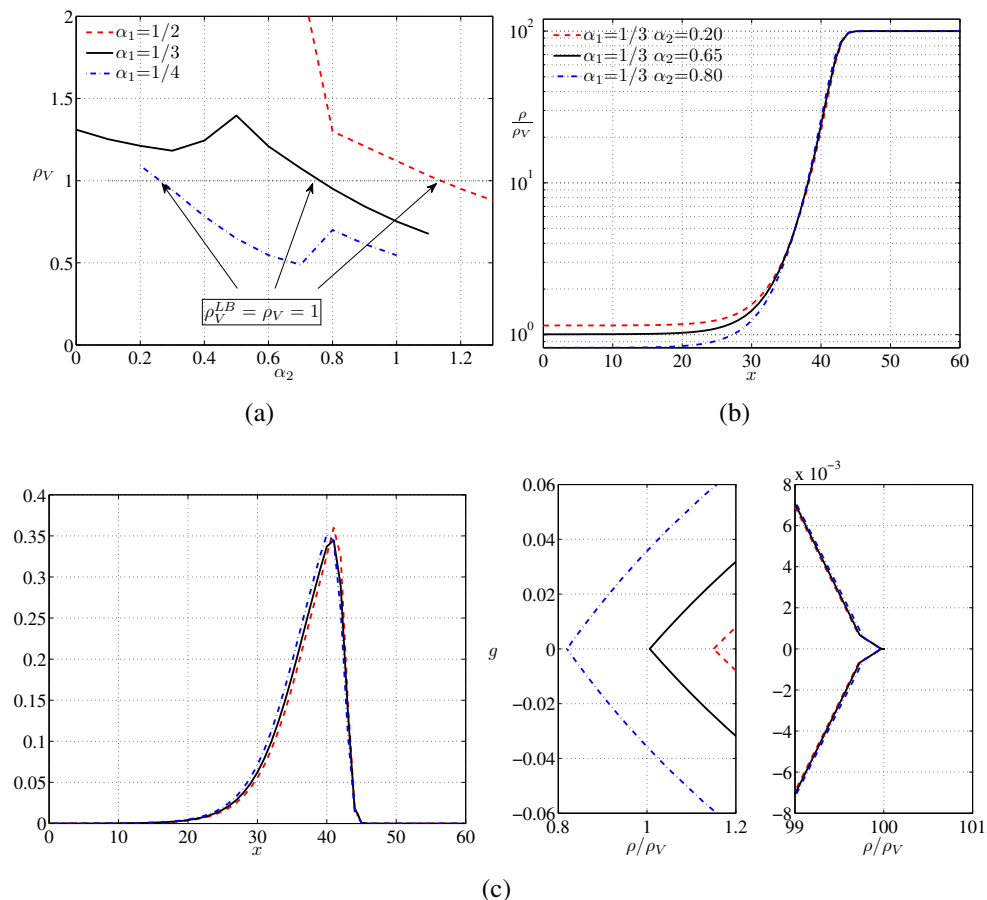


Figure 3: Customized EOS and phase equilibrium in simulation of a flat interface;  $\rho_L=100$ ,  $\rho_V = 1$ ,  $\tau = 1.0$ . (a) Perturbation parameters leading to agreement with continuum predictions. (b) Density profile  $\rho(x)$  in semilog plot (left side). (c) In all panels,  $g$  is the normal component of the internal force. The leftmost panel in (c) shows the spatial variation of  $g(x)$  when crossing the interface ( $g>0$  points towards the denser phase). The two rightmost panels in (c) show the internal force variation with respect to mass density (or the excess free-energy density  $F^{EX} = g(\rho)$ ). The correct densities for liquid-vapor coexistence are recovered in each phase bulk for  $\alpha_2=0.65$  and  $\int_{\rho_V}^{\rho_L} g(\rho)d\rho = \theta \log(\rho_L/\rho_V)=3.07$ .

a fixed  $\alpha_1$ , that satisfies the following form of chemical equilibrium

$$\Delta\mu^{LB}(\alpha_1, \alpha_2) = \int_{\mathbf{x}(\rho_V)}^{\mathbf{x}(\rho_L)} \mathbf{g} \cdot d\mathbf{x} - \theta \log(\rho_L/\rho_V) = 0; \quad (39)$$

above  $\mathbf{x}$  is a general coordinate along the direction normal to the interface. For this purpose we employ quasi-Newton method <sup>(29)</sup> that runs along the LB simulation to solve Eq. (39). The success of the iterative Newton method  $\alpha_2^k = \alpha_2^{k-1} + \Delta\alpha$  is highly sensitive to the initial value  $\alpha_2^0$  and the maximum step size  $|\Delta\alpha|$ . In order to identify good initial guesses for the studied system we performed a series of LB simulations for fixed values of  $\alpha_1$  and  $\alpha_2$  and different step sizes; proper initialization parameters are reported in Table 3 along with the EOS parameters for different density ratios. The effect of the step size on the convergence rate is shown in Figure 4. Starting from proper initial guesses the solver converges monotonically for small step sizes  $\Delta\alpha$ . The long times observed for convergence is caused by a strong initial shock due to wrong initialization of the density profile that excite long-lasting acoustic modes that only decay after several relaxation times. As the Newton iteration evolves we observe that the work done by internal forces or chemical potential excess  $\Delta\mu^{EX} = \int_{\mathbf{x}(\rho_V)}^{\mathbf{x}(\rho_L)} \mathbf{g} \cdot d\mathbf{x}$  is exactly balanced out by diffusion so that  $\Delta\mu^{EX} = \Delta\mu^{IG} = \theta \log(\rho_L/\rho_V)$  as  $\rho_V^{LB} \rightarrow \rho_V = 1$ .

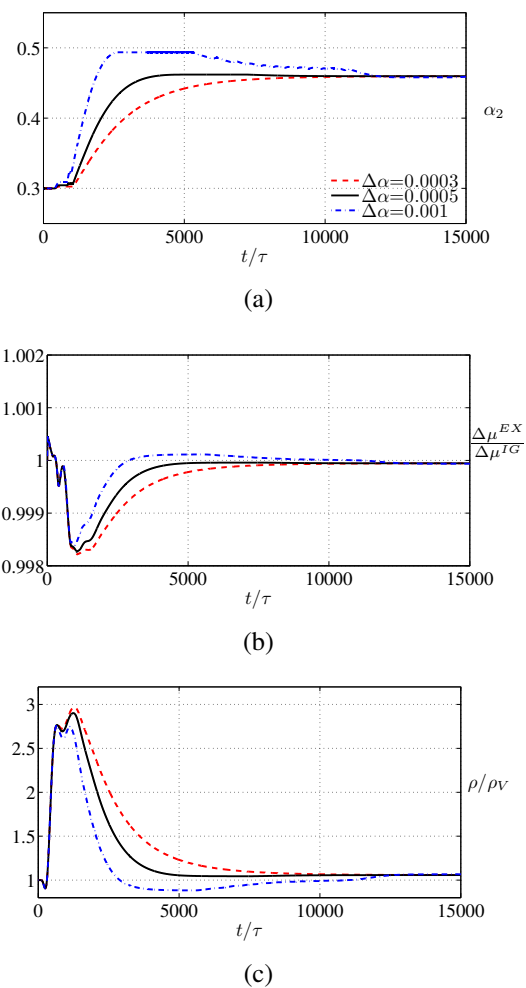


Figure 4: Quasi-Newton solver convergence for a flat interface simulation ( $\rho_L = 1000, \rho_V = 1, \tau = 1.5$ ) using three different parameter increments  $\Delta\alpha = 0.0003, 0.0005,$  and  $0.001$ . The subfigures show time traces for: (a) perturbation parameter  $\alpha_2$ ; (b) chemical potential excess  $\Delta\mu^{EX} = \int_{\mathbf{x}(\rho_V)}^{\mathbf{x}(\rho_L)} \mathbf{g} \cdot d\mathbf{x}$  normalized by  $\Delta\mu^{IG} = \theta \log(\rho_L/\rho_V)$ ; and (c) mass density in the vapor phase normalized by  $\rho_V$ .

## 5 Results & Discussion

For the study in point we adopt  $\rho_V = 1$  in all cases while  $\rho_L=10,100$  &  $1000$ ). In all cases, the speed of sound for the vapour phase is  $\sqrt{\theta_V} = 0.2c_s$  while  $\sqrt{\theta_L} = c_s$  in the liquid phase, and the magnitude of slope in unstable branch is  $\theta_S = -0.36c_s^2$ .

We perform a series of simulation of flat and circular interfaces adopting the proposed methodology employing a range of relaxation times ( $1 \leq \tau \leq 2$ ) for which the local Froude number is less than unit  $Fr = \tau|\mathbf{g}(\mathbf{x})|/\sqrt{\theta} < 1$ .

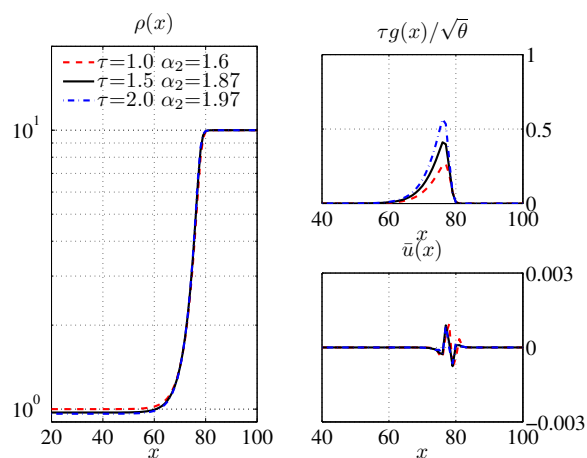
### 5.1 Flat interface

The simulation of a flat interface is performed in a **doubly periodic domain (i.e. periodic in both  $x$  and  $y$  directions) of dimension  $L_x = 201 \times L_y = 3$** . The  $x$ -direction is normal to the interface and the integration in Eq. (39) can be easily performed across the two interfaces that develop within the simulation domain. We focus on phase separation at three different density ratios, namely 1:10, 1:100, and 1:1000, employing the EOS reported in Table 3. The density field has been initialized with a relatively smooth profile in the interface between the vapour and liquid phases. An interface becomes stable after few time steps and reaches steady state, with no observable variations in the interface shape nor thickness, after 10000 relaxation times. The density profiles shown in Figures 5a–c show that the interface thickness is nearly constant ( $\approx 20$  lattice sites) for all simulated density ratios. This highlights that the employed EOS with constant negative slope

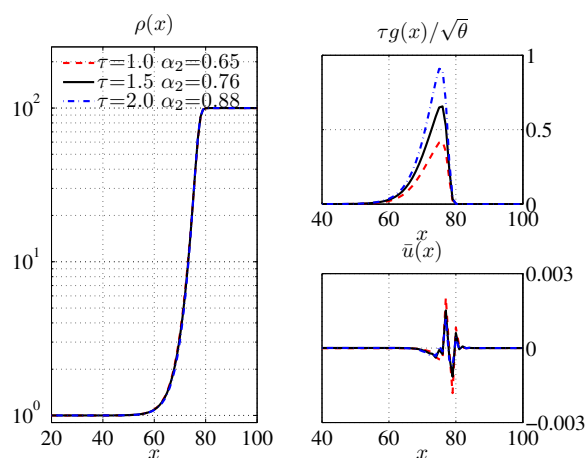
( $\theta_S = 0.6$ ) in the unstable branch leads to high surface tensions as the density contrast increases; this will be quantified in the next subsection. As reported in Figure 5, the local Froude number remains below unit in the present simulations for the adopted relaxation times. The half-time-step, or hydrodynamical, velocity field  $\mathbf{u}_{hs} = \mathbf{u}_{hs} - 0.5\mathbf{g}$  shows that spurious currents are extremely small for the flat interface case.

## 5.2 Circular droplet

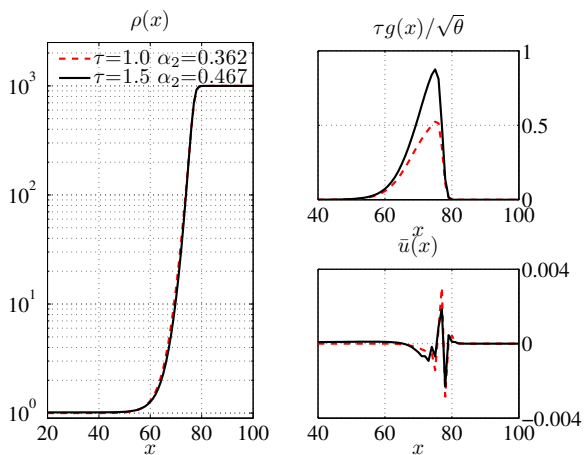
A series of simulations of a liquid droplet formation in a bulk vapour phase, has been performed. To check consistency with continuum thermodynamics for circular interfaces, we compare our numerical results against the Laplace equation in Figure 6, and thermodynamic equilibrium (Kelvin's equation) in Figure 7. While the Laplace equation can only determine the pressure drop  $\Delta p = p_L - p_V = \gamma/R$ , one needs to impose both mechanical equilibrium, shifted by  $\Delta p = \gamma/R$ , and chemical equilibrium in order to predict the coexistence densities  $\rho_V^R$  and  $\rho_L^R$  in the presence of a circular interface of radius  $R$ . For the adopted equations of state, the solution of  $\rho_V^R$  and  $\rho_L^R$  can be readily obtained via integration of the EOS, i.e. without the classic ideal gas approximation for the vapour phase and incompressible behaviour in the liquid; the results are reported in Figure 7 along with numerical simulation. The present simulations report high values of the surface tension and the expected linear behaviour  $\Delta p \propto 1/R$  for radii greater than the interface thickness  $R \geq 20$ . Meanwhile, the increase in the saturation vapour pressure  $\rho_V^R$  due to curvature effects is numerically reproduced within a 5–8% error in all



(a)



(b)



(c)

Figure 5: Flat interface simulation: density profile in semilog plot (left panels), local Froude number (upper right panels), and half-step velocity field  $\mathbf{u}_{hs} = \mathbf{u}_{hs} - 0.5\mathbf{g}$  (lower right panels). (a)  $\rho_L/\rho_V = 10$ . (b)  $\rho_L/\rho_V = 100$ . (c)  $\rho_L/\rho_V = 1000$ .

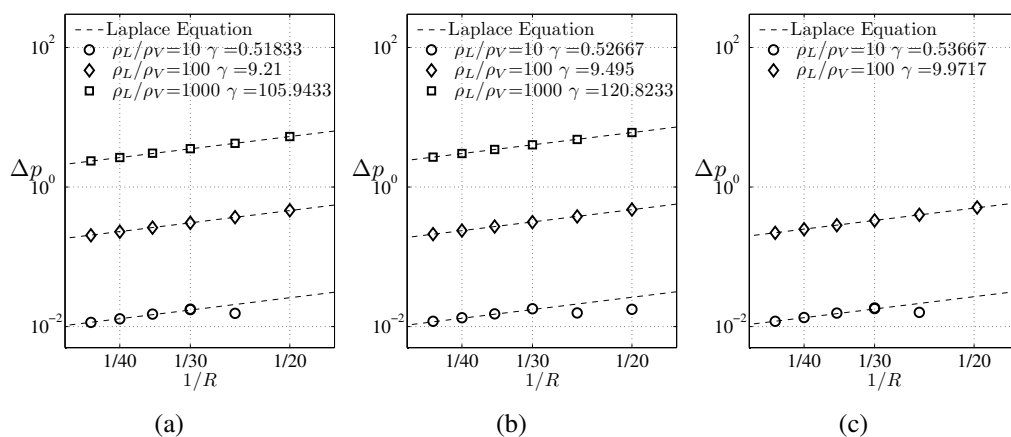


Figure 6: Surface tension measured via Laplace’s equation. (a)  $\tau=1.0$  (b)  $\tau=1.5$ . (c)  $\tau=2.0$ .

cases. One of the main by-products of inaccuracies in LB simulations is the presence of spurious currents; that is artificial currents due to finite-order isotropy of the lattice. As discussed in previous work, these currents are proportional to the density ratio between the phases <sup>(5)</sup>. In recent years, several recipes have been proposed to tame the problem of spurious currents in the multiphase LB scenario, both for free energy and the pseudo-potential approaches <sup>(30,31)</sup>. Even for the highest density ratio of 1:1000, the proposed EOS gives rise to relatively small spurious currents, as reported in Figure 8. The highest spurious velocities take place near the interface of the droplet and the recirculation structures observed are affected by the shape and size of the simulation domain. **Since increasing dissipation helps reducing the observed currents ( i.e.  $|\mathbf{u}_{max}| \sim \mathcal{O}(10^{-2})$  for  $\tau = 1.0$ ,  $|\mathbf{u}_{max}| \sim \mathcal{O}(10^{-3})$  for  $\tau = 1.5$ ), a higher Froude number for higher  $\tau$  (see Figure 8b) may not necessarily result in a higher magnitude of the spurious currents.**

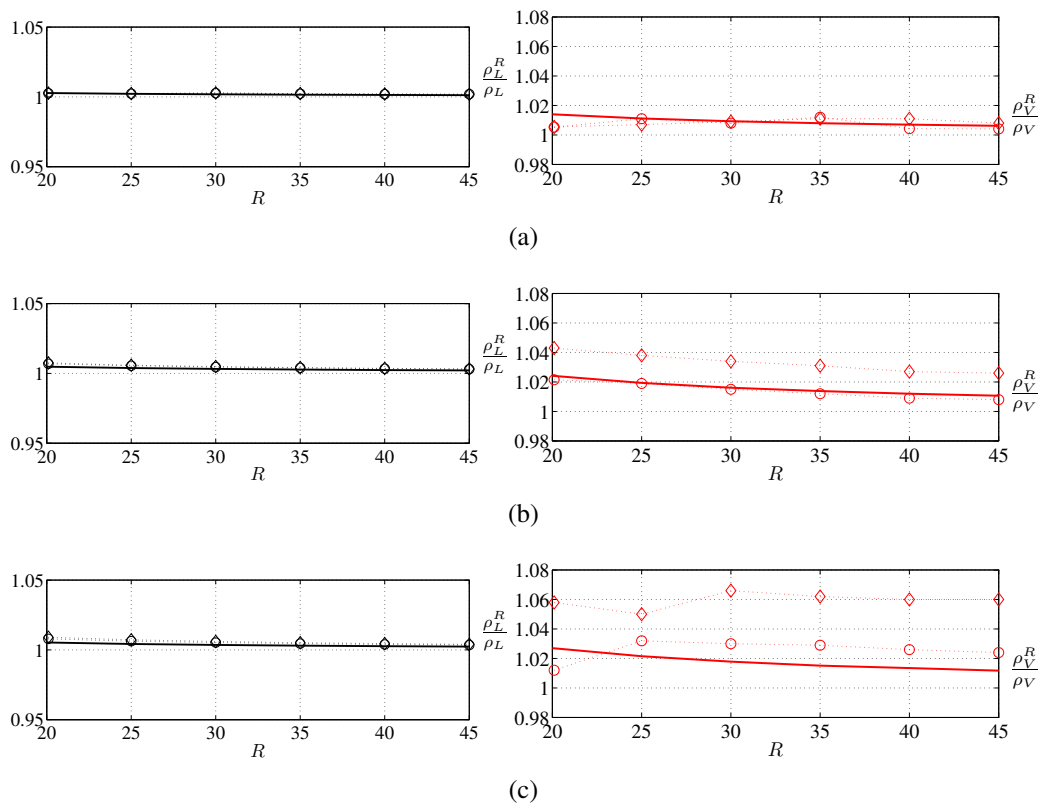
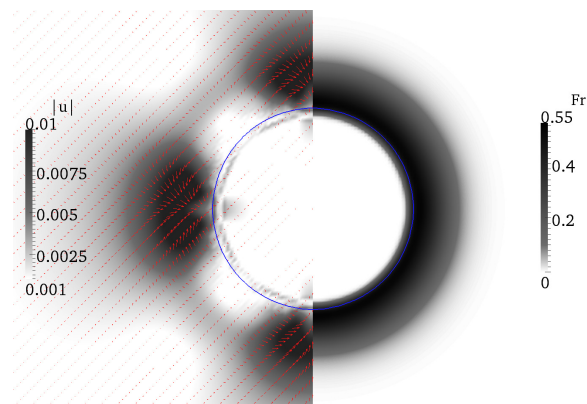
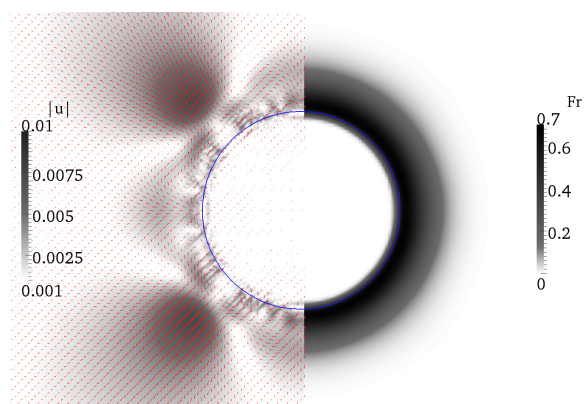


Figure 7: Thermodynamic equilibrium for a circular interface of radius  $R$ . The figures compare numerical results for the coexistence densities  $\rho_L^R$  and  $\rho_V^R$  against predictions from the Kelvin equation. (a)  $\rho_L/\rho_V=10$ . (b)  $\rho_L/\rho_V=100$ . (c)  $\rho_L/\rho_V=1000$ .

In any case, the maximum value of  $|\mathbf{u}| \sim \mathcal{O}(10^{-2})$ , did not compromise numerical stability.



(a)



(b)

Figure 8: Circular interface: velocity field at half-time-step and local Froude number for very high density ratio,  $\rho_L/\rho_V=1000$ . (a)  $\tau = 1.0$  ( $|\mathbf{u}_{max}| \simeq 0.01$ ). (b)  $\tau = 1.5$  ( $|\mathbf{u}_{max}| \simeq 0.005$ ).

## 6 Conclusions

We have presented a second-order LB scheme for non-ideal fluids in isothermal conditions that achieves stable phase-separation for large density ratios  $\rho_L/\rho_V$  and large (isothermal) compressibility ratios  $\beta_V/\beta_L = \rho_L\theta_L/\rho_V\theta_V$ .

**The basic observation in this work is that it is possible to adjust the equation of state (EOS) in the unstable segment (spinodal region) without affecting thermodynamic properties in the phase bulk. This permits to achieve a better compliance with continuum thermodynamics, without affecting the numerical stability of the scheme.**

Employing an alternative approach to the Chapman-Enskog expansion, we derived the closed-form macroscopic equations that result from the (second-order) LB model employed which relies on an explicit scheme for the force term. The detailed derivation of the macroscopic equations indicates that the pressure and stress tensors contain terms that can lead to substantial numerical error when the magnitude of applied forces is large (i.e.  $Fr = \tau|\mathbf{g}/\sqrt{\theta}| \sim 1$ ). Accommodating sufficient number of nodes within the interface constitutes the simplest optimization strategy to deal with physical conditions that are demanding for simulation. This strategy can be readily performed by scaling the slopes of the proposed EOS with respect to the lattice temperature  $\theta$ . This approach, however, can come at the expense of a large computational cost. **The conditions chosen to demonstrate the proposed methodology represent a challenging situation for multiphase flow simulation, given the very high density and compressibility ratios em-**

employed. Nevertheless, the scheme in this work achieved stable phase separation for density ratios up to 1 : 1000 by using moderate-to-high, but still affordable, grid resolutions.

The present results rest on two crucial features of the employed method: (i) compliance with Galerkin representation to second-order in Hermite space which is secured by projection of the post-advection distribution function; (ii) mechanical and thermodynamical consistency achieved through self-tuning of the unstable (spinodal) branch of the EOS, while leaving the stable ones completely unaffected.

The proposed tuning of the EOS requires an iterative feedback loop in order to minimize an objective function. The objective function in this work is given by the equality of chemical potentials on both sides of the vapor-liquid interface. Such equality of chemical potentials across the vapor-liquid interface is attained when the specific work (per unit mass) performed by internal forces is equal to the specific work done by thermal diffusion. The self-tuning allows to dynamically compensate for any discretization errors that can become significant near the interface. At the same time, the EOS in the bulk is not affected since corrections to the EOS are only applied to the unstable branch. In practice, the procedure adjusts the internal forces on the light phase side of the interface where one usually observes large numerical discrepancies between bulk densities predicted via Maxwell's construction and those obtained by LB simulation.

In the present implementation, a high-order lattice with sixth-order isotropy

was adopted in order to reduce spurious currents and other effects related to lack of isotropy of high-order spatial derivatives in the discrete gradient operator employed for computing the internal forces. The method is numerically demonstrated for flat and circular interfaces at rest, for density ratios in the range 1 : 10 to 1 : 1000 and compressibility ratios of 250 : 1 and 25000 : 1, always showing satisfactory agreement with analytical predictions and small contamination due to spurious interface currents.

The proposed methodology can circumvent the resort to higher-order Hermite projections and/or implicit schemes. For the two cases studied here, with simple interface geometries, the proposed optimization procedure can be readily implemented. The extension of the presented approach to moving and deforming interfaces makes an interesting subject of future research work.

It is hoped and felt that the dynamic optimization strategy presented in this work will permit robust LB simulation of multiphase flows with high density contrasts, such as air-water systems.

## **7 Acknowledgements**

Valuable discussions with M. Sbragaglia and Y.G. Kevrekidis are kindly acknowledged.

## References

- [1] S. Succi, *The Lattice Boltzmann Equation for Fluid Dynamics and Beyond*, Clarendon, Oxford, 2001.
- [2] L. Biferale, P. Coveney, S. Ubertini and S. Succi, *Phil. Trans. Roy. Soc. A*, 2011, **369**, 2384–2386.
- [3] X. Shan and H. Chen, *Phys. Rev. E*, 1993, **47**, 1815–1820.
- [4] A. Kupershtokh, D. Medvedev and D. Karpov, *Comp. Math. App.*, 2009, **58**, 965–974.
- [5] P. Yuan and L. Schaefer, *Physics of Fluids*, 2006, **18**, 042101.
- [6] R. Zhang, X. Shan and H. Chen, *Phys. Rev. E*, 2006, **74**, 046703.
- [7] C. E. Colosqui, *Phys. Rev. E*, 2010, **81**, 026702.
- [8] J. Latt and B. Chopard, *Math. and Comp. Sim.*, 2006, **72**, 165–168.
- [9] C. E. Colosqui, H. Chen, X. Shan, I. Staroselsky and V. Yakhot, *Phys. Fluids*, 2009, **21**, 013105.
- [10] M. R. Swift, E. Orlandini, W. R. Osborn and J. M. Yeomans, *Phys. Rev. E*, 1996, **54**, 5041–5052.
- [11] X. Shan, *Phys. Rev. E*, 2006, **73**, 047701.
- [12] P. Rosenau, *Phys. Lett. A*, 1986, **118**, 222–227.

- [13] V. Yakhot and C. E. Colosqui, *J. Fluid Mech.*, 2007, **586**, 249–258.
- [14] X. He, G. Doolen and T. Clark, *J. Comput. Phys.*, 2002, **179**, 439–451.
- [15] M. Sbragaglia, R. Benzi, L. Biferale, S. Succi, K. Sujiyama and F. Toschi, *Phys. Rev. E*, 2007, **75**, 026702.
- [16] R. Benzi, S. Succi and M. Vergassola, *Phys. Rep.*, 1992, **222**, 145–197.
- [17] Z. Guo, C. Zheng and B. Shi, *Phys. Rev. E*, 2002, **65**, 046308.
- [18] N. Martys, X. Shan and H. Chen, *Phys. Rev. E*, 1998, **58**, 6855.
- [19] J. Buick and C. Greated, *Phys. Rev. E*, 2000, **61**, 5307.
- [20] Z. Guo and G. Zheng, *Phys. Rev. E*, 2002, **65**, 046308.
- [21] G. Falcucci, G. Chiatti, S. Succi, A. Mohamad and A. Kuzmin, *Phys. Rev. E*, 2009, **79**, 056706.
- [22] A. Mohamad and A. Kuzmin, *Int. J. Heat and Mass Trans.*, 2010, **53**, 990.
- [23] M. Swift, W. Osborne and J. Yeomans, *Phys. Rev. Lett.*, 1995, **75**, 830.
- [24] M. Sbragaglia, R. Benzi, L. Biferale, H. Chen, X. Shan and S. Succi, *J. Fluid Mech.*, 2009, **628**, 299–309.
- [25] J. M. Yeomans, *Physica A*, 2006, **369**, 159–184.
- [26] S. Melchionna and U. Marini Bettolo Marconi, *Euro Phys. Lett.*, 2008, **81**, 34001.

- [27] U. Marini Bettolo Marconi and S. Melchionna, *J. Chem. Phys.*, 2009, **131**, 014105.
- [28] X. Shan, X. Yuan and H. Chen, *J. Fluid Mech.*, 2006, **550**, 413–441.
- [29] C. Kelley and E. Sachs, *SIAM J. Control Optim.*, 1987, **25**, 1503–1516.
- [30] G. Falcucci, S. Ubertini and S. Succi, *Soft Matter*, 2010, **6**, 4357–4365.
- [31] G. Falcucci, S. Ubertini, C. Biscarini, S. Di Francesco, D. Chiappini, S. Pappacelli, A. De Maio and S. Succi, *Comm. Comput. Phys.*, 2011, **9**, 269–296.